COMPARATIVE DYNAMIC ANALYSIS OF TILTROTOR DRIVE TRAIN CONFIGURATIONS USING THE TRANSFER MATRIX METHOD

Bo Li[*,†,+], Pierangelo Masarati[†], Xiao Wang[*]
[*]Nanjing University of Aeronautics and Astronautics, Nanjing, China
[†]Politecnico di Milano, Milan, Italy

ABSTRACT

This paper presents a general torsional modeling and analysis approach based on the Transfer Matrix Method applicable to tiltrotor drive train configurations. A novel transfer matrix model for the rotating blade's lead-lag mode is derived and integrated to establish coupled rotor-drivetrain-engine dynamic models. Based on XV-15 tiltrotor, three distinct drive train configurations are developed. The modal results of representative configuration obtained by the proposed method are validated against flight test data and the Finite Element Method, demonstrating a close agreement for both helicopter and airplane modes. The dynamic analysis reveals that the transition between flight modes has negligible impact on the torsional mode of the drive train system. Furthermore, minor architectural differences, such as the tilting mechanism, do not significantly alter the dynamic characteristics. However, a major change in engine layout, from a dual-engine, side-by-side arrangement to a single, centered engine, results in a markable shift in the natural frequency of the system.

NOTATION

*

Symbols

EI Bending stiffness, Nm^2

f Frequency, Hz

GJ_p Torsional stiffness, Nm^2

K Stiffness matrix

l Length of shaft, m

m Mass per unit span, kg/m

M Mass matrix

M_y, M_z Bending moments, Nm

Q_y, Q_z Shear force, N

r_h Radius of the hub

R Radius of the rotor

T Torque, Nm

$\mathbf{U}$ Transfer matrix

v Lagwise displacement, m

w Flapwise displacement, m

$\mathbf{z}$ State vector

Δ Determinate symbol

θ Angular displacement, rad

ρ Mass density, kg/m

ω Natural frequency, rad/s

Ω Rotation speed, r/min

*

Acronyms

VTOL Vertical Take-Off and Landing

NGCTR Next-Generation Civil Tiltrotor

TMM Transfer Matrix Method

FEM Finite Element Method

INTRODUCTION

Tiltrotor aircraft combine the best features of helicopters and fixed-wing aircraft: the ability to perform vertical takeoff and landing (VTOL) operations while achieving high-speed cruise. By overcoming key limitations of conventional rotorcraft and fixed-wing aircraft, they are becoming indispensable for military and civilian applications. Thus, they are considered a promising solution for aviation transportation in the 21st century.

Currently, the only tiltrotor aircraft in service is a military model, the Bell Boeing V-22 (Ref. 1), with Bell's V-280 (Ref. 2) at an advanced development stage, including renaming it MV-75, while earlier experimental models included Bell's XV-3 (Ref. 3) and XV-15 (Ref. 4). In the civil aviation sector, Leonardo's AW609 (Ref. 5), the research initiative Next-Generation Civil Tiltrotor (NGCTR) (Refs. 6, 7), and the recently revealed United Aircraft R6000[1] represent pioneering advances in tiltrotor technology. These aircraft feature various configurations of drive train systems, which are more complex and potentially more safety-critical than those of conventional helicopters.

Existing tiltrotor aircraft typically utilize a symmetric drive train architecture featuring dual gearboxes linked by an interconnecting shaft, which provides continuous power distribution and rotation synchronization between the rotors. At the same time, the center gearbox connecting both sides of the transmission system ensures flight safety in case of engine failure (Refs. 8, 9). These drive train configurations for tiltrotor aircraft can be divided into three types, characterized by the location of the engine(s) and what portion of the rotor-gearbox-engine assembly tilts. The engines can be located (1) in the fuselage (as in the single-engine Bell XV-3), or (2, 3) in pods at the wing tips. In the former case, only the rotors tilt. In the latter case, the engine nacelles can either tilt along with the rotors (2) or remain fixed, while only the rotors tilt (3). The first configuration (Fig. 1(a)) was utilized only in the early days of tiltrotor research for the XV-3, with a single engine located in the fuselage, transmitting power to the tip-mounted rotors via a drive train. The second configuration (Fig. 1(b)) is the most common, seen in the XV-15, V-22, and AW609, where both the engine nacelles and rotors tilt. The third configuration (Fig. 1(c)), used in the Bell V-280 and Leonardo NGCTR, keeps the engine nacelles fixed while allowing only the rotors to tilt. Due to relatively abundant publicly available data and literature on Bell XV-15's drive train, which could be used as a reference, the drive trains of configuration (1) and (3) are derived from configuration (2). In configurations (2) and (3), interconnecting shafts connect the two engines via a center gearbox. A variant of configuration (1), with two engines embedded at the wing root driving the tilting rotors through a drive train along the wing, is being proposed by Leonardo Helicopter in a new conceptual study for an Advanced Tiltrotor Aircraft (ATA) (Ref. 10).

[1] https://www.asianmilitaryreview.com/2024/10/china-unveils-large-tiltrotor-uav-protoype/, accessed October 2024.

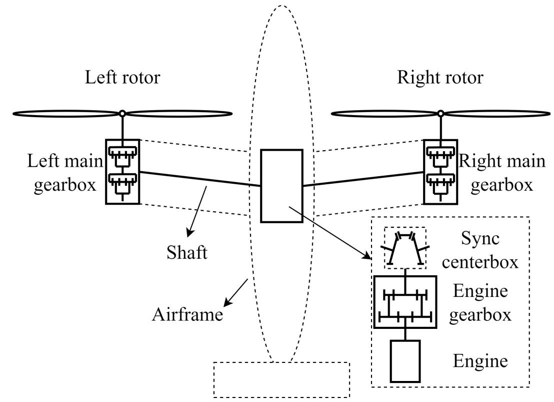

(a) Configuration 1

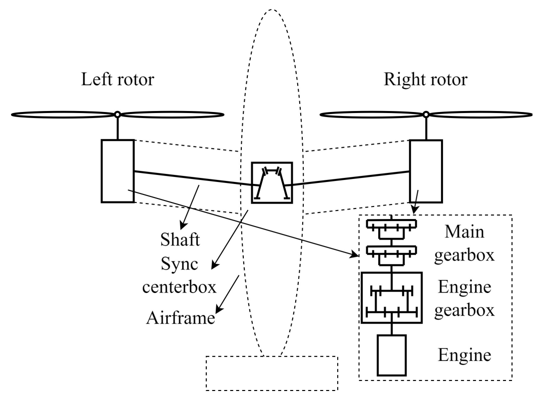

(b) Configuration 2

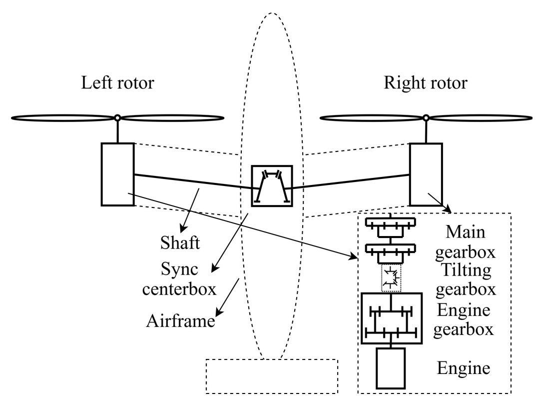

(c) Configuration 3

Figure 1: Three types of tiltrotor drive train configuration.

The drive train is a critical component in rotorcraft due to its central role in power transmission. It connects the engines to the rotors, transmitting power to generate thrust for lift while operating in helicopter mode and propulsion during flight in airplane mode. The dynamic interaction between the engines, rotors, and drive train components creates challenges for torsional modeling and dynamic analysis. Coupling effects may lead to torsional instability, excessive vibration in the rotor and drive components, or degraded vehicle handling qualities (Refs. 11, 12). This is a critical concern during the preliminary design phase of tiltrotor aircraft because dynamic interface problems at the drive train level risk remaining undetected until later development stages, making corrections costly.

In terms of mechanical system modeling and analysis, the most common computational methods are the finite element method (FEM) and the transfer matrix method (TMM). The FEM excels in analyzing multi-dimensional systems through spatial discretization. However, large-scale dynamic problems with extensive degrees of freedom lead to high computational costs. Conversely, the TMM provides a computationally efficient framework for one-dimensional systems, such as torsional systems. Instead of assembling large coupled governing equations, it propagates state vectors throughout the drive train system using transfer matrices, significantly reducing computational complexity. The modular structure of this method makes it well-suited for drive train dynamic problems.

MODELING METHODS

Transfer Matrix Method

Tiltrotor drive trains are fundamentally composed of drive shafts, gearboxes, and additional components that couple engines to rotors. This forms a typical one-dimensional torsional multibody system, for which the TMM is ideally suited. The TMM stems from an idea first introduced by Holzer in 1921 (Ref. 13) and subsequently popularized in the rotorcraft community by Myklestad in 1945 (Ref. 14). Myklestad's approach to the bending-torsion analysis of rotating shafts was further extended and used for the eigenanalysis of entire rotor blades at a time of limited computational resources. The method was revitalized in later years by Rui et al. (Refs. 15, 16), who extended it to general multibody dynamics problems. Recent applications to helicopter rotor and drive train dynamics include (Refs. 17, 18).

The basic idea of TMM is to break up a complicated multibody system into elements containing bodies and joints with dynamics properties expressed in matrix form. The overall transfer matrix can be derived by successive multiplications of matrices of individual elements and assembling them according to the topology structure of the system. The characteristic equation is then obtained from the overall transfer equation by enforcing the system's boundary conditions.

The state vector of a torsional vibration system under physical coordinates is given by

$$\mathbf{z}_{i,j} = \begin{bmatrix} \theta & T \end{bmatrix}^T \tag{1}$$

where θ is angular displacement and T is torque.

A library of transfer matrices of various elements widely used in multibody systems is provided in (Ref. 16). The transfer matrix of an elastic shaft with a uniform cross-section in a torsional vibration system is defined as

$$\mathbf{U}_i(x) = \begin{bmatrix} \cos\gamma x & \dfrac{\sin\gamma x}{\gamma GJ} \\ -\gamma GJ \sin\gamma x & \cos\gamma x \end{bmatrix} \tag{2}$$

where $0 < x \leq \ell$ is a generic point at spanwise section x, ℓ is the length of the shaft, $\gamma = \sqrt{\rho J_p \omega^2/(GJ_p)}$, GJ_p is the torsional stiffness of the shaft cross-section, and J_p is the polar inertia moment of the shaft cross-section. For massless shafts (i.e., of negligible inertia, when ω is low enough that $0 \approx \gamma \ll 1$), the transfer matrix can be further simplified as

$$\mathbf{U}_i = \begin{bmatrix} 1 & \dfrac{\ell}{GJ_p} \\ 0 & 1 \end{bmatrix} \tag{3}$$

The transfer matrix of a rigid disk with inertia J is defined as

$$\mathbf{U}_i = \begin{bmatrix} 1 & 0 \\ -\omega^2 J & 1 \end{bmatrix} \tag{4}$$

In this study, gears are assumed to be kinematically and dynamically ideal. This implies that the compliance of the gear teeth is neglected, and phenomena such as non-smooth contact dynamics and ripple effects are not taken into account. Power losses due to friction and similar factors are also beyond the scope of this work. A geared system can be treated as a purely one-dimensional system.

A typical directed acyclic graph system in topology form is shown in Fig. 2(a), with two branches joining together at the element labeled "3". Typically, a general drive train can be treated as a system composed of multiple directed chains. The acyclic graph system can be split into a combination of simple chain graphs by introducing additional connection elements.

Fig. 2 intuitively describes the transfer relationship and transfer direction of each element's state vector. Circles denote body elements, and arrows denote the transfer direction of the state vector. For convenience, all elements are numbered in sequence. In a multibody system, only one arbitrary boundary end is indicated as the root, whereas other endpoints in the remaining system boundaries are considered as tips. In Fig. 2(a), the element labeled "1" is chosen as the root, and the elements labeled "5" and "7" are considered tips.

In a chain system, the overall transfer equation can be obtained directly by simple matrix multiplications and written as $\mathbf{z}_\mathrm{O} = \mathbf{U}_i \mathbf{z}_\mathrm{I}$, where $\mathbf{U}_i$ represents the relationship between the input end $\mathbf{z}_\mathrm{I}$ and the output end $\mathbf{z}_\mathrm{O}$. However, for a directed acyclic graph system, the junction between chains requires specialized treatment. Fig. 2(b) illustrates the derivation of the overall transfer equation of the two-branched directed acyclic graph system. Thus, we obtain

$$\begin{aligned} \mathbf{z}_{1,0} &= \mathbf{U}_1\mathbf{U}_2\left(\mathbf{U}_3\mathbf{U}_4\mathbf{U}_5\mathbf{z}_{5,0} + \mathbf{U}_{6,3}\mathbf{U}_6\mathbf{U}_7\mathbf{z}_{7,0}\right) \\ &= \mathbf{U}_1\mathbf{U}_2\mathbf{U}_3\mathbf{U}_4\mathbf{U}_5\mathbf{z}_{5,0} + \mathbf{U}_1\mathbf{U}_2\mathbf{U}_{6,3}\mathbf{U}_6\mathbf{U}_7\mathbf{z}_{7,0} \end{aligned} \tag{5}$$

Rotating Blade Transfer Matrix

The static rotor blade can be simplified as an Euler-Bernoulli cantilever beam. The blade is discretized into uniform cross-section continuous rotating beam elements as shown in Fig. 3(a), and respective topology structure in Fig. 3(b).

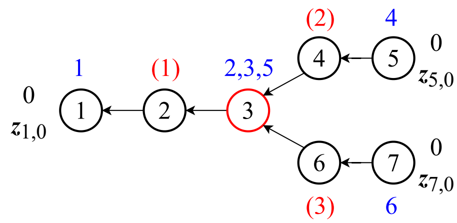

(a) Topology of acyclic graph system

$$z_{4,3}=\boldsymbol{U}_4 z_{5,4} \longleftarrow z_{5,4}=\boldsymbol{U}_5 z_{5,0} \longleftarrow z_{5,0}$$

$$z_{1,0}=\boldsymbol{U}_1 z_{2,1} \longleftarrow z_{2,1}=\boldsymbol{U}_2 z_{3,2} \longleftarrow z_{3,2}=\boldsymbol{U}_3 z_{4,3}+\boldsymbol{U}_{6,3} z_{6,3}$$

$$z_{6,3}=\boldsymbol{U}_6 z_{7,6} \longleftarrow z_{7,6}=\boldsymbol{U}_7 z_{7,0} \longleftarrow z_{7,0}$$

(b) Transfer equation deduction

Figure 2: Topology of a typical directed acyclic graph system.

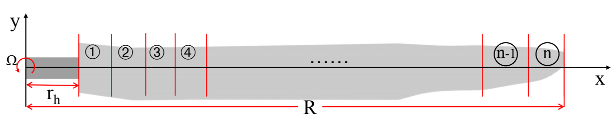

(a) Model of the rotating blade

(b) Topology of rotating blade

Figure 3: Discretization of a rotating blade.

The rotation of the beam induces centrifugal and Coriolis forces, resulting in a transfer matrix that differs from that of a static system. Based on the previous work (Refs. 17, 18), the transfer matrix of the rotating beam element can be derived as follows. The free vibration equations of lagwise and flapwise motion can be expressed as

$$\begin{cases} \dfrac{\partial}{\partial x^2}\left[EI_{zz}\dfrac{\partial^2 V}{\partial x^2}\right]-\dfrac{\partial}{\partial x}\left[P\dfrac{\partial V}{\partial x}\right]-m\Omega^2 V+m\dfrac{\partial^2 V}{\partial t^2}=0 \\ \dfrac{\partial}{\partial x^2}\left[EI_{yy}\dfrac{\partial^2 W}{\partial x^2}\right]-\dfrac{\partial}{\partial x}\left[P\dfrac{\partial W}{\partial x}\right]+m\dfrac{\partial^2 W}{\partial t^2}=0 \end{cases} \tag{6}$$

where EI_{zz} is the lagwise bending stiffness, EI_{yy} is the flapwise bending stiffness, m is the mass per unit span, P is the axial force resulting from the integration of the distributed centrifugal loads, $P=\int_x^R m\Omega^2(r_h+x)\mathrm{d}x$, R is the rotor radius, Ω is the rotor angular velocity, and r_h is the radius of the hub.

Assume variable separation and an exponential time dependence $V(x,t)=v(x)e^{i\omega t}$ and $W(x,t)=w(x)e^{i\omega t}$ into Eq. (6) to obtain differential equations. The state vector of rotating beam undergoing lagwise and flapwise vibration is

$$\mathbf{z}=\begin{bmatrix} v & w & \theta_z & \theta_y & M_z & M_y & Q_y & Q_z \end{bmatrix}^T \tag{7}$$

where v,w are the lagwise and flapwise displacements, θ_z,θ_y are the slopes of beam, M_z,M_y are the bending moments, Q_y,Q_z are the shear forces.

The transfer matrix of the rotating beam element is

$$\mathbf{U}_i=\begin{bmatrix} a_1 & c_1 & a_2 & c_2 & a_3 & c_3 & a_4 & c_4 \\ a_1' & c_1' & a_2' & c_2' & a_3' & c_3' & a_4' & c_4' \\ EIa_1'' & EIc_1'' & EIa_2'' & EIc_2'' & EIa_3'' & EIc_3'' & EIa_4'' & EIc_4'' \\ b_1 & d_1 & b_2 & d_2 & b_3 & d_3 & b_4 & d_4 \end{bmatrix} \tag{8}$$

where

$s_1=\sqrt{\frac{\sqrt{P^2+4(\Omega^2+\omega^2)m_0EI}}{2EI}+P}$,

$s_2=\sqrt{\frac{\sqrt{P^2+4(\Omega^2+\omega^2)m_0EI}}{2EI}-P}$,

$s_3=\sqrt{\frac{\sqrt{P^2+4\omega^2m_0EI}}{2EI}+P}$, $s_4=\sqrt{\frac{\sqrt{P^2+4\omega^2m_0EI}}{2EI}-P}$,

$a_1=\frac{s_1^2\cos ls_2+s_2^2\cosh ls_1}{s_1^2+s_2^2}$, $a_2=\frac{\Gamma_1\sinh ls_1+\Gamma_2\sin ls_2}{\Lambda_1}$,

$a_3=\frac{\cosh s_1-\cos ls_2}{EI\left(s_1^2+s_2^2\right)}$, $a_4=\frac{s_1s_2(s_2\sinh ls_1-s_1\sin ls_2)}{\Lambda_1}$,

$b_1=\frac{s_1^2\Gamma_1\sin ls_2+s_2^2\Gamma_2\sinh ls_1}{s_1s_2\left(s_1^2+s_2^2\right)}$, $b_2=\frac{\Gamma_1\Gamma_2(\cosh ls_1-\cos ls_2)}{s_1s_2\Lambda_1}$,

$b_3=\frac{\Gamma_2\sinh ls_1-\Gamma_1\sin ls_2}{EIs_1s_2\left(s_1^2+s_2^2\right)}$, $b_4=\frac{s_1\Gamma_1\cos ls_2+s_2\Gamma_2\cosh ls_2}{\Lambda_1}$,

$c_1=\frac{s_3^2\cos ls_4+s_4^2\cosh ls_3}{s_3^2+s_4^2}$, $c_2=\frac{\Gamma_3\sinh ls_3+\Gamma_4\sin ls_4}{\Lambda_2}$,

$c_3=\frac{\cosh s_3-\cos ls_4}{EI\left(s_3^2+s_4^2\right)}$, $c_4=\frac{s_3s_4(s_4\sinh ls_3-s_3\sin ls_4)}{\Lambda_2}$,

$d_1=\frac{s_3^2\Gamma_3\sin ls_4+s_4^2\Gamma_4\sinh ls_3}{s_3s_4\left(s_3^2+s_4^2\right)}$, $d_2=\frac{\Gamma_3\Gamma_4(\cosh ls_3-\cos ls_4)}{s_3s_4\Lambda_2}$,

$d_3=\frac{\Gamma_4\sinh ls_3-\Gamma_3\sin ls_4}{EIs_3s_4\left(s_3^2+s_4^2\right)}$, $d_4=\frac{s_3\Gamma_3\cos ls_4+s_4\Gamma_4\cosh ls_4}{\Lambda_2}$,

$\Gamma_1=EIs_1s_2^4+Ps_1s_2^2+\Omega^2m_0s_1$,

$\Gamma_2=EIs_2s_1^4-Ps_2s_1^2+\Omega^2m_0s_2$,

$\Gamma_3=EIs_3s_4^4+Ps_3s_4^2$,

$\Gamma_4=EIs_4s_3^4-Ps_4s_3^2$,

$\Lambda_1=EIs_1^4s_2^2+EIs_1^2s_2^4+\Omega^2m_0s_1^2+\Omega^2m_0s_2^2$,

$\Lambda_2=EIs_3^4s_4^2+EIs_3^2s_4^4$.

The symbols $'$ and $''$ indicate the first- and second-order partial derivatives with respect to l, treating l as a variable.

The overall transfer matrix of a rotating blade, discretized into n beam elements, can be written as

$$\mathbf{U}_{\text{blade}}=\mathbf{U}_1\mathbf{U}_2\ldots\mathbf{U}_{n-1}\mathbf{U}_n \tag{9}$$

The main structural data (Ref. 19), namely the mass and chordwise and flapwise stiffness distributions of each beam element of the discretized rotor blade are shown in Fig. 4.

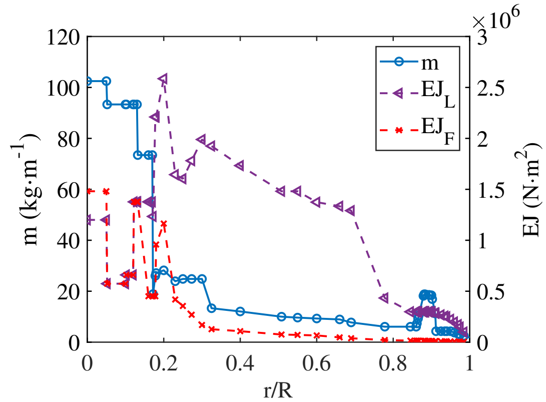

Figure 4: Blade properties.

Critical Speed of Supported Shaft

Typically, the interconnecting shafts are supported by multiple single-row grease-packed and sealed hanger bearings. The bending vibrations and critical speeds of rotating shafts are among the most challenging issues in vibration analysis, posing persistent difficulties in mechanical design and maintenance. The critical speed of a rotating shaft refers to the rotational speed at which severe transverse vibrations occur. Operating a shaft at this speed is highly dangerous, as the increasing vibration amplitude can lead to structural failure. Therefore, avoiding these critical speeds is essential to ensuring the reliability and safety of tiltrotor drive trains.

The interconnecting shaft is supported by 2 hanger bearings at 1/3 length and 2/3 length and can be divided into 5 elements, as shown in Fig. 5.

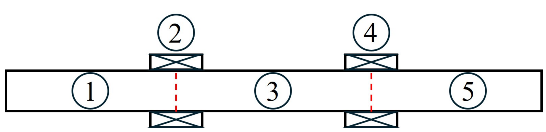

Figure 5: Shaft supported by bearings.

The state vector of the shaft is $\mathbf{z}_{i,j} = \begin{bmatrix} y & \theta_z & M_z & Q_y \end{bmatrix}^T$. The transfer matrix of the shaft element is given as

$$\mathbf{U}_{\text{shaft}} = \begin{bmatrix} 1 & l_i & \frac{l_i^2}{2EI_i} & \frac{l_i^3}{6EI_i} \\ 0 & 1 & \frac{l_i^2}{2EI_i} & \frac{l_i^3}{6EI_i} \\ 0 & 0 & 1 & l_i \\ 0 & 0 & 0 & 1 \end{bmatrix} \tag{10}$$

The bearing transmits forces and moments while restricting displacement. Thus, the transfer matrix of the bearing element is expressed as

$$\mathbf{U}_{\text{bearing}} = \begin{bmatrix} 0 & 0 & 0 & 0 \\ 0 & 1 & 0 & 0 \\ 0 & 0 & 1 & 0 \\ 0 & 0 & 0 & 1 \end{bmatrix} \tag{11}$$

The transfer equation of the bearing-supported interconnecting shaft can be obtained by multiplication of transfer matrices of all elements

$$\mathbf{z}_{\text{O}} = \mathbf{U}_1\mathbf{U}_2\mathbf{U}_3\mathbf{U}_4\mathbf{U}_5\mathbf{z}_{\text{I}} \tag{12}$$

where $U_i(i = 1,3,5)$ is transfer matrix of shaft element, $U_j(j = 2,4)$ is transfer matrix of bearing element.

By considering boundary conditions at two ends that $M_z = 0, Q_y = 0$ and y, θ_z are non-zero, we obtain a determinant from Eq. (12)

$$\Delta = \begin{vmatrix} \mathrm{u}_{11} & \mathrm{u}_{12} \\ \mathrm{u}_{21} & \mathrm{u}_{22} \end{vmatrix} = 0 \tag{13}$$

Transfer Equations for Drive Trains

The respective topology figures for Fig. 1 is drawn in Fig. 6. The blade is discretized into 8 beam elements, thus the transfer matrix can be obtained based on Eq. (14) as

$$\mathbf{U}_{\text{blade}} = \mathbf{U}_{B_{11}} \ldots \mathbf{U}_{B_{17}}\mathbf{U}_{B_{18}} \tag{14}$$

Other blades have the same expression as Eq. (14). The two-stage planetary gearbox can be considered as a whole component, and the corresponding transfer matrix is expressed as

$$\mathbf{U}_{\text{PG}} = \mathbf{U}_4\mathbf{U}_5\mathbf{U}_6\mathbf{U}_7\mathbf{U}_8 \tag{15}$$

The overall transfer equations for the coupled drive train can be directly obtained by matrix multiplications according to the topology structures in Fig. 7.

$$\begin{bmatrix} \mathbf{U}_{c1} & \mathbf{U}_{c2} & \mathbf{U}_{c3} & \mathbf{U}_{c4} & \mathbf{U}_{c5} & \mathbf{U}_{c6} & -\mathbf{I} \\ \mathbf{U}_{g1} & -\mathbf{U}_{g2} & \mathbf{0} & \mathbf{0} & \mathbf{0} & \mathbf{0} & \mathbf{0} \\ \mathbf{0} & \mathbf{U}_{g2} & -\mathbf{U}_{g3} & \mathbf{0} & \mathbf{0} & \mathbf{0} & \mathbf{0} \\ \mathbf{0} & \mathbf{0} & \mathbf{U}_{g3'} & -\mathbf{U}_{g4'} & -\mathbf{U}_{g5'} & -\mathbf{U}_{g6'} & \mathbf{0} \\ \mathbf{0} & \mathbf{0} & \mathbf{0} & \mathbf{U}_{g4} & -\mathbf{U}_{g5} & \mathbf{0} & \mathbf{0} \\ \mathbf{0} & \mathbf{0} & \mathbf{0} & \mathbf{0} & \mathbf{U}_{g5} & -\mathbf{U}_{g6} & \mathbf{0} \end{bmatrix} \begin{Bmatrix} \mathbf{z}_{\text{B18,0}} \\ \mathbf{z}_{\text{B28,0}} \\ \mathbf{z}_{\text{B38,0}} \\ \mathbf{z}_{\text{B48,0}} \\ \mathbf{z}_{\text{B58,0}} \\ \mathbf{z}_{\text{B68,0}} \\ \mathbf{z}_{1,0} \end{Bmatrix} = \mathbf{0} \tag{16}$$

where $\mathbf{U}_{c1} = \mathbf{U}_1\mathbf{U}_2\mathbf{U}_3\mathbf{U}_11\mathbf{U}_10\mathbf{U}_{\text{PG}}\mathbf{U}_9\mathbf{U}_{\text{blade}_1}$,
$\mathbf{U}_{c2} = \mathbf{U}_1\mathbf{U}_2\mathbf{U}_3\mathbf{U}_11\mathbf{U}_10\mathbf{U}_{\text{PG}}\mathbf{U}_V\mathbf{U}_{\text{blade}_2}$,
$\mathbf{U}_{c3} = \mathbf{U}_1\mathbf{U}_2\mathbf{U}_3\mathbf{U}_11\mathbf{U}_10\mathbf{U}_{\text{PG}}\mathbf{U}_V\mathbf{U}_{\text{blade}_3}$,
$\mathbf{U}_{c4} = \mathbf{U}_1\mathbf{U}_2\mathbf{U}_3\mathbf{U}_V\mathbf{U}_12\mathbf{U}_{\text{PG}}\mathbf{U}_{21}\mathbf{U}_{\text{blade}_4}$,
$\mathbf{U}_{c5} = \mathbf{U}_1\mathbf{U}_2\mathbf{U}_3\mathbf{U}_V\mathbf{U}_12\mathbf{U}_{\text{PG}}\mathbf{U}_V\mathbf{U}_{\text{blade}_5}$,
$\mathbf{U}_{c6} = \mathbf{U}_1\mathbf{U}_2\mathbf{U}_3\mathbf{U}_V\mathbf{U}_12\mathbf{U}_{\text{PG}}\mathbf{U}_V\mathbf{U}_{\text{blade}_6}$,
$\mathbf{U}_{g1} = \mathbf{U}_G\mathbf{U}_{\text{blade}_1}$, $\mathbf{U}_{g2} = \mathbf{U}_G\mathbf{U}_{\text{blade}_2}$, $\mathbf{U}_{g3} = \mathbf{U}_G\mathbf{U}_{\text{blade}_3}$,
$\mathbf{U}_{g3'} = \mathbf{U}_G\mathbf{U}_{10}\mathbf{U}_{\text{PG}}\mathbf{U}_V\mathbf{U}_{\text{blade}_3}$,
$\mathbf{U}_{g4} = \mathbf{U}_G\mathbf{U}_{\text{blade}_4}$, $\mathbf{U}_{g4'} = \mathbf{U}_G\mathbf{U}_{12}\mathbf{U}_{\text{PG}}\mathbf{U}_{21}\mathbf{U}_{\text{blade}_4}$,
$\mathbf{U}_{g5} = \mathbf{U}_G\mathbf{U}_{\text{blade}_5}$, $\mathbf{U}_{g5'} = \mathbf{U}_G\mathbf{U}_{12}\mathbf{U}_{\text{PG}}\mathbf{U}_V\mathbf{U}_{\text{blade}_5}$,
$\mathbf{U}_{g6} = \mathbf{U}_G\mathbf{U}_{\text{blade}_6}$, $\mathbf{U}_{g6'} = \mathbf{U}_G\mathbf{U}_{12}\mathbf{U}_{\text{PG}}\mathbf{U}_V\mathbf{U}_{\text{blade}_6}$.

Table 1: Gear ratios for drive trains.

Components	Configuration 1	Configuration 2,3
Engine - Engine gearbox	19846:8487	19846:8487
Engine gearbox - Planetary gearbox	/	8487:565
Engine gearbox - Center gearbox	8487:6392	8487:6392
Center gearbox - Planetary gearbox	6392:565	/

Table 2: Equivalent inertia of each component in the drive train system.

Component	Mode	Engine		Engine gearbox	Planetary gearbox	Center gearbox	Hub
		Config 1	Config 2,3				
Inertia	Helicopter mode	27.5705	13.7852	11.8159	11.5247	0.9847	0.0543
($\times 10^9$ kg $\cdot$ m^2)	Airplane mode	18.1244	9.0622	7.7676	7.5757	0.6473	0.0357

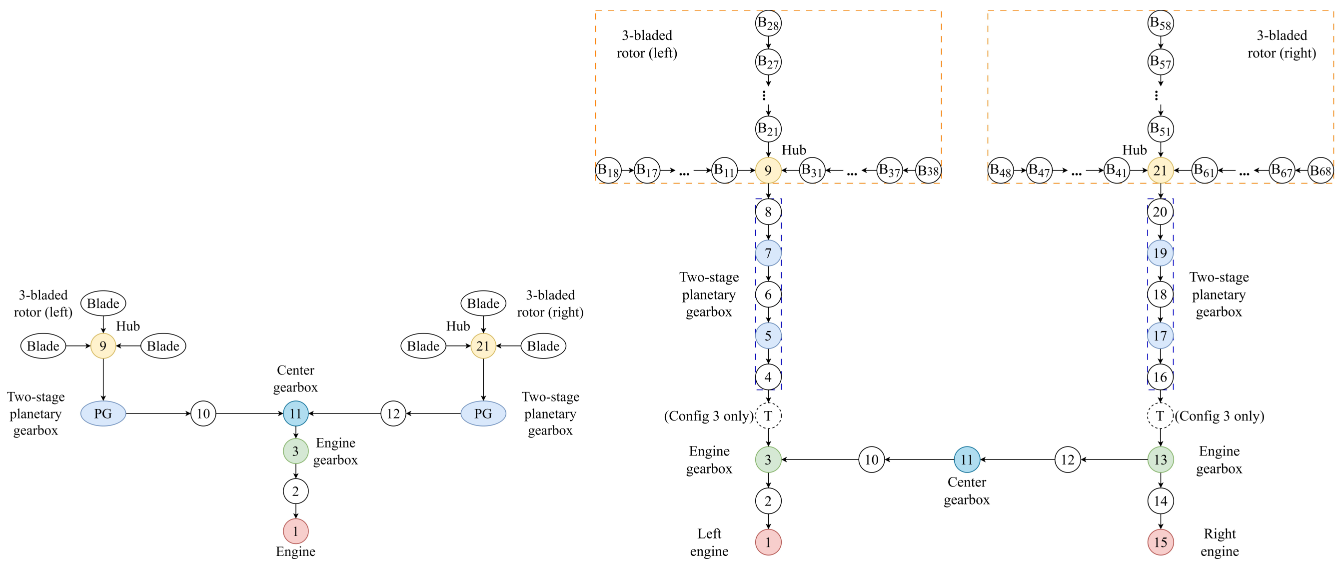

(a) configuration 1 (b) configuration 2,3

Figure 6: Topology figure of drive trains.

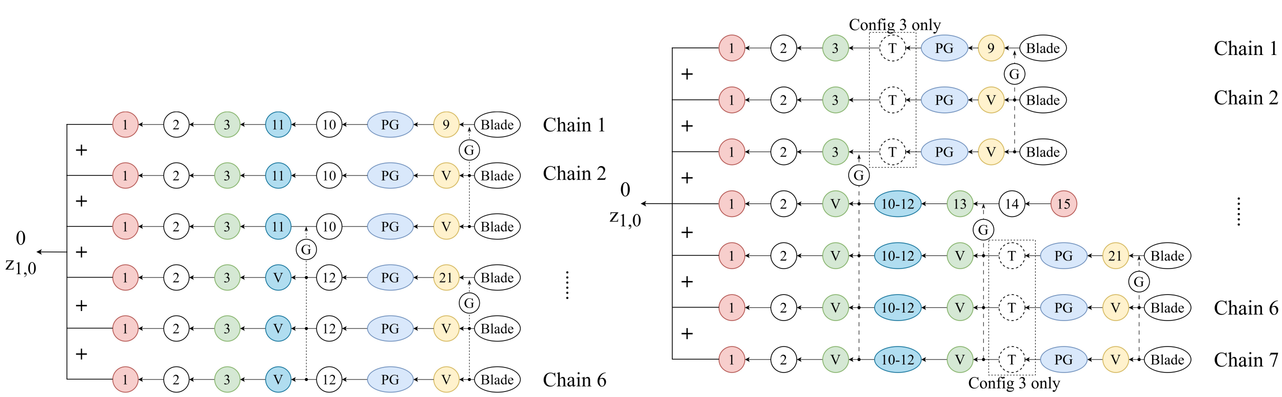

(a) configuration 1 (b) configuration 2,3

Figure 7: Topology figure of drive trains decoupled into directed chains.

$$
\begin{bmatrix}
\mathbf{U}_{c1} & \mathbf{U}_{c2} & \mathbf{U}_{c3} & \mathbf{U}_{c4} & \mathbf{U}_{c5} & \mathbf{U}_{c6} & \mathbf{U}_{c7} & -\mathbf{I} \\
\mathbf{U}_{g1} & -\mathbf{U}_{g2} & \mathbf{0} & \mathbf{0} & \mathbf{0} & \mathbf{0} & \mathbf{0} & \mathbf{0} \\
\mathbf{0} & \mathbf{U}_{g2} & -\mathbf{U}_{g3} & \mathbf{0} & \mathbf{0} & \mathbf{0} & \mathbf{0} & \mathbf{0} \\
\mathbf{0} & \mathbf{0} & \mathbf{U}_{g3'} & -\mathbf{U}_{g4'} & -\mathbf{U}_{g5''} & -\mathbf{U}_{g6''} & -\mathbf{U}_{g7''} & \mathbf{0} \\
\mathbf{0} & \mathbf{0} & \mathbf{0} & \mathbf{U}_{g4} & -\mathbf{U}_{g5'} & -\mathbf{U}_{g6'} & -\mathbf{U}_{g7'} & \mathbf{0} \\
\mathbf{0} & \mathbf{0} & \mathbf{0} & \mathbf{0} & \mathbf{U}_{g5} & -\mathbf{U}_{g6} & \mathbf{0} & \mathbf{0} \\
\mathbf{0} & \mathbf{0} & \mathbf{0} & \mathbf{0} & \mathbf{0} & \mathbf{U}_{g6} & -\mathbf{U}_{g7} & \mathbf{0}
\end{bmatrix}
\begin{Bmatrix}
\mathbf{z}_{B18,0} \\ \mathbf{z}_{B28,0} \\ \mathbf{z}_{B38,0} \\ \mathbf{z}_{15,0} \\ \mathbf{z}_{B48,0} \\ \mathbf{z}_{B58,0} \\ \mathbf{z}_{B68,0} \\ \mathbf{z}_{1,0}
\end{Bmatrix}
= \mathbf{0} \quad (17)
$$

where

$\mathbf{U}_{c1} = \mathbf{U}_1\mathbf{U}_2\mathbf{U}_3\mathbf{U}_T\mathbf{U}_{\text{PG}}\mathbf{U}_9\mathbf{U}_{\text{blade}_1}$,

Table 3: Equivalent torsional stiffness of each component's output shaft in drive train system.

Output shaft	Mode	Engine		Engine gearbox	Planetary gearbox	Center gearbox
		Config 1	Config 2,3			
Torsional stiffness GJ	Helicopter mode	15.9132	7.9566	0.3604	0.0003	0.0211
($\times 10^{15}$ N $\cdot$ m^2)	Airplane mode	10.4612	5.2306	0.2369	0.0002	0.0139

$\mathbf{U}_{c2} = \mathbf{U}_1\mathbf{U}_2\mathbf{U}_3\mathbf{U}_T\mathbf{U}_{\text{PG}}\mathbf{U}_V\mathbf{U}_{\text{blade}_2}$,
$\mathbf{U}_{c3} = \mathbf{U}_1\mathbf{U}_2\mathbf{U}_3\mathbf{U}_T\mathbf{U}_{\text{PG}}\mathbf{U}_V\mathbf{U}_{\text{blade}_3}$,
$\mathbf{U}_{c4} = \mathbf{U}_1\mathbf{U}_2\mathbf{U}_V\mathbf{U}_{10-15}$,
$\mathbf{U}_{c5} = \mathbf{U}_1\mathbf{U}_2\mathbf{U}_V\mathbf{U}_{10-12}\mathbf{U}_V\mathbf{U}_T\mathbf{U}_{\text{PG}}\mathbf{U}_{21}\mathbf{U}_{\text{blade}_4}$,
$\mathbf{U}_{c6} = \mathbf{U}_1\mathbf{U}_2\mathbf{U}_V\mathbf{U}_{10-12}\mathbf{U}_V\mathbf{U}_T\mathbf{U}_{\text{PG}}\mathbf{U}_V\mathbf{U}_{\text{blade}_5}$,
$\mathbf{U}_{c7} = \mathbf{U}_1\mathbf{U}_2\mathbf{U}_V\mathbf{U}_{10-12}\mathbf{U}_V\mathbf{U}_T\mathbf{U}_{\text{PG}}\mathbf{U}_V\mathbf{U}_{\text{blade}_6}$,
$\mathbf{U}_{g1} = \mathbf{U}_G\mathbf{U}_{\text{blade}_1}$, $\mathbf{U}_{g2} = \mathbf{U}_G\mathbf{U}_{\text{blade}_2}$, $\mathbf{U}_{g3} = \mathbf{U}_G\mathbf{U}_{\text{blade}_3}$,
$\mathbf{U}_{g3'} = \mathbf{U}_G\mathbf{U}_T\mathbf{U}_{\text{PG}}\mathbf{U}_V\mathbf{U}_{\text{blade}_3}$,
$\mathbf{U}_{g4} = \mathbf{U}_G\mathbf{U}_{14}\mathbf{U}_{15}$, $\mathbf{U}_{g4'} = \mathbf{U}_G\mathbf{U}_{10-15}$,
$\mathbf{U}_{g5} = \mathbf{U}_G\mathbf{U}_{\text{blade}_4}$, $\mathbf{U}_{g5'} = \mathbf{U}_G\mathbf{U}_T\mathbf{U}_{\text{PG}}\mathbf{U}_{21}\mathbf{U}_{\text{blade}_4}$,
$\mathbf{U}_{g5''} = \mathbf{U}_G\mathbf{U}_{10-12}\mathbf{U}_V\mathbf{U}_T\mathbf{U}_{\text{PG}}\mathbf{U}_{21}\mathbf{U}_{\text{blade}_4}$,
$\mathbf{U}_{g6} = \mathbf{U}_G\mathbf{U}_{\text{blade}_5}$, $\mathbf{U}_{g6'} = \mathbf{U}_G\mathbf{U}_T\mathbf{U}_{\text{PG}}\mathbf{U}_V\mathbf{U}_{\text{blade}_5}$,
$\mathbf{U}_{g6''} = \mathbf{U}_G\mathbf{U}_{10-12}\mathbf{U}_V\mathbf{U}_T\mathbf{U}_{\text{PG}}\mathbf{U}_V\mathbf{U}_{\text{blade}_5}$,
$\mathbf{U}_{g7} = \mathbf{U}_G\mathbf{U}_{\text{blade}_6}$, $\mathbf{U}_{g7'} = \mathbf{U}_G\mathbf{U}_T\mathbf{U}_{\text{PG}}\mathbf{U}_V\mathbf{U}_{\text{blade}_6}$,
$\mathbf{U}_{g7''} = \mathbf{U}_G\mathbf{U}_{10-12}\mathbf{U}_V\mathbf{U}_T\mathbf{U}_{\text{PG}}\mathbf{U}_V\mathbf{U}_{\text{blade}_6}$.
When $\mathbf{U}_T$ is eliminated, the general overall transfer equation degenerates to that of configuration 2.

Finite Element Method

For verification, a simple, lumped parameter model based on the Finite Element Method (FEM) is set up for one of the configurations.

The method is based on defining the rotation of each node i, θ_i, with $i = 1..N_J$, the corresponding inertia moments, J_i, the connectivity of each shaft j, θ_{j_1} and θ_{j_2}, where j_1 and j_2 represent the indexes of the two nodes the shaft connects, with $j = 1..N_k$, and the corresponding shaft stiffnesses, $k_j = GJ_j/\ell_j$.

After collecting the connectivities in the "incidence matrix" $\mathbf{S} \in \mathbb{R}^{N_k \times N_J}$, such that the difference between the rotations at the two ends of each shaft, $\Delta\theta_j = \theta_{j_2} - \theta_{j-1}$, is represented by setting $\mathbf{S}_{j,j_2} = 1$ and $\mathbf{S}_{j,j_1} = -1$, one obtains $\Delta\theta = \mathbf{S}\theta$.

Defining the mass matrix as $\mathbf{M} = \text{diag}(J_i)$ and the stiffness matrix as $\hat{\mathbf{K}} = \text{diag}(k_j)$, with $\mathbf{M} \in \mathbb{R}^{N_J \times N_J}$ and $\hat{\mathbf{K}} \in \mathbb{R}^{N_k \times N_k}$, the virtual work of the inertia and elastic forces is

$$\begin{aligned} 0 = \delta\mathcal{W} &= -\delta\theta^T\mathbf{M}\ddot{\theta} - \delta\Delta\theta^T\hat{\mathbf{K}}\Delta\theta \\ &= -\delta\theta^T\left(\mathbf{M}\ddot{\theta} + \mathbf{S}^T\hat{\mathbf{K}}\mathbf{S}\theta\right) \end{aligned} \tag{18}$$

i.e., by considering the arbitrariness of virtual rotations, redefining $\mathbf{K} = \mathbf{S}^T\hat{\mathbf{K}}\mathbf{S}$ and replacing $\ddot{\theta} = s^2\theta$ one obtains the standard second-order generalized eigenproblem

$$\left(s^2\mathbf{M} + \mathbf{K}\right)\theta = \mathbf{0} \tag{19}$$

The model parameters J_i and k_j should be adjusted to obtain an equivalent model in which all elements have the same rotational velocity. This can be achieved by using the rotational velocity of the first element as a reference. The equivalent stiffness and inertia of the other elements should thus be scaled by the square of the corresponding velocity ratios.

RESULTS AND DISCUSSION

Validation

The dynamic models for various tiltrotor drive train configurations have been established according to the modeling method outlined in Section MODELING METHODS.
The general equation of the system can be described as

$$\mathbf{U}_{\text{all}}\mathbf{z}_{\text{all}} = \mathbf{0} \tag{20}$$

In a drive train torsional vibration system, natural boundary conditions corresponding to zero torques, $T = 0$, are assumed at the free ends, resulting in the elimination of half of the state variables. Eq. 20 thus reduces to

$$\bar{\mathbf{U}}_{\text{all}}\bar{\mathbf{z}}_{\text{all}} = \mathbf{0} \tag{21}$$

where vector $\bar{\mathbf{z}}_{\text{all}}$ only contains the remaining boundary state variables corresponding to displacements, and matrix $\bar{\mathbf{U}}_{\text{all}}$ consists of the original matrix $\mathbf{U}_{\text{all}}$ after elimination of the unnecessary rows and columns.

The eigenfrequency of the system can be obtained by solving the determinant of $\bar{\mathbf{U}}$ equals zero, e.g., $\det(\bar{\mathbf{U}}) = 0$.

Gear ratios, equivalent inertia of each component, and equivalent torsional stiffness of each component's output shaft in the drive train system are given in Table 1-3 respectively. Based on configuration 2, some assumptions are made to simplify the other two configurations, which are modeled with similar properties. Configuration 1 features a single engine, with its inertia and torsional stiffness of its output shaft set to twice that of configuration 2. The tilting mechanism of configuration 3 is assumed to possess the same inertia as the center gearbox.

The proposed method for drive train system modeling and analysis is validated by comparing simulation results of configuration 2 with flight test data from existing literature (Ref. 20), as well as results obtained by FEM (Ref. 21), which is briefly introduced in Subsection Finite Element Method. The eigenfrequencies of the drive train (configuration 2) are computed and listed in Table 4 for comparison, with respective torsional mode shapes shown in Fig. 8 and Fig. 9. It can be found that the results obtained by the present method closely align with both the flight test data and results from

FEM, thereby illustrating the effectiveness and accuracy of the proposed method. After numerical validation, the eigenvalues of the other two configurations are calculated. Eigenfrequencies for single-engine tiltrotor drive train (configuration 1) and only rotor-tilting drive train (configuration 3) are illustrated in Table. 5. Torsional mode shapes for configuration 1 and configuration 2 in helicopter and airplane modes are presented in Fig. 10-11 and Fig. 12-13 respectively.

Vibration Characteristics of Drive Train

The modal analyses have been conducted in multiple flight modes. According to the results, it can be found that the rotation speed slightly affects the natural frequencies in the operational range. The coupling of the rotor collective lagwise modes is considered; similar frequencies can thus be found in the torsional frequencies of the drive train system shown in Table 4. The torsional mode shapes of the drive train system, as depicted in Fig. 8-13, demonstrate symmetric or antisymmetric patterns due to the inherent structural symmetry of the tiltrotor aircraft configuration.

In the case of the twin-engine tiltrotor configurations (configurations 2 and 3), the first and fifth modes are mainly dominated by the rotor collective lagwise oscillation modes. The second and third modes, respectively showing symmetry and asymmetry, are both primarily dominated by the engine and main gearbox modes. For the interconnecting shaft and center gearbox, they only affect the torsional system in symmetric modes. The difference between the two configurations lies in the tilting mechanism, however, it does not significantly influence the torsional modes of the drive train system. On the other hand, for the single-engine tiltrotor configuration (configuration 1), the first four modes are predominantly governed by the rotor collective lagwise oscillation modes. The fifth mode is primarily influenced by the center gearbox. The layout of the engine and engine gearbox in configuration 1 results in a different torsional mode shape compared to configurations 2 and 3, which is reflected in the eigenfrequencies listed in Table 5.

CONCLUSIONS

In this study, a comprehensive coupled rotor-drivetrain-engine dynamic model was developed based on TMM and the novel and versatile approach was validated by comparing eigenfrequencies from existing literature and FEM for configuration 2, showing a good agreement. Comparative dynamic analysis of tiltrotor drive train configurations were conducted in both helicopter and airplane modes. The main conclusions are as follows:

1. The dynamic analysis revealed that the torsional mode shapes of tiltrotor drive train systems exhibit symmetric or antisymmetric patterns, a direct consequence of the inherent structural symmetry of drive train.

2. For dual-engine configurations, the dominant dynamic behaviors were identified. The tilting mechanism was found to have a negligible effect on the overall torsional modes.

3. In single-engine configuration, the engine layout significantly changes the dynamic characteristics. It highlights a distinct difference in modal behavior compared to the dual-engine configurations.

The developed approach for dynamic modeling and analysis approach is an efficient and effective tool for preliminary design phase of tiltrotor in terms of torsional dynamic evaluation of drive train system. For future work, the model will be extended to include fully coupled rotating blade dynamics to further improve accuracy. Furthermore, a sensitivity analysis of eigenvalues will be performed based on TMM to provide valuable guidance for tiltrotor drive train deisign and optimization.

Author contact:
Bo Li bo.li@polimi.it libo663@nuaa.edu.cn
Pierangelo Masarati pierangelo.masarati@polimi.it
Xiao Wang x.wang@nuaa.edu.cn

ACKNOWLEDGMENTS

The first author is supported by the China Scholarship Council program (202306830074).

REFERENCES

1. Dimitri A. Dousis, L. Brent Giles, R. Keith Hale, and Thomas B. Priest. V-22 drive train vibration monitoring system ground station development. In *American Helicopter Society 55th Annual Forum*, pages 1–18, Montreal, Canada, May 25–27 1999.

2. Ryan Ehinger, Matt McMenemy, and Paul Wilson. Bell V-280 Valor: A flight test update. In *Vertical Flight Society 74th Annual Forum*, pages 1–13, Phoenix, AZ, USA, May 14–17 2018. https://doi.org/10.4050/F-0074-2018-12904.

3. W. H. Deckert and R. G. Ferry. Limited flight evaluation of the XV-3 aircraft. Report AFFTC-TR-60-4, Air Force Flight Test Center, May 1960.

4. Daniel C. Dugan, Ronald G. Erhart, and Laurel G. Schroers. The XV-15 tilt rotor research aircraft. TM 81244, NASA, 1980.

5. Alberto Trezzini. AW609 civil tiltrotor drive train torsional stability analysis and certification test campaign. In *the Vertical Flight Society's 77th Annual Forum & Technology Display*, pages 1–8, Palm Beach, FL, USA, May 11–13 2021. https://doi.org/10.4050/F-0077-2021-16772.

6. Carlo Cassinelli, Pierre Abdel Nour, Gianni Bernini, Gabriele Campanardi, Maria Dall'Aglio, Cristian Lilliu, Matteo Pecoraro, and Gaetano Preatoni. Experimental aerodynamics validation of a tiltrotor platform within next generation tiltrotor technology demonstrator project. In *Vertical Flight Society's 79th Annual Forum & Technology Display*, West Palm Beach, FL, USA, May 16–18 2023. https://doi.org/10.4050/F-0079-2023-18003.

Table 4: Frequencies of drive train system (configuration 2), unit: Hz.

Method	Mode	f_1	f_2	f_3	f_4	f_5
Present (TMM)	Helicopter mode	3.78	12.15	13.59	32.23	33.75
	Airplane mode	3.78	12.15	13.56	32.19	33.69
Ref. 20	Helicopter mode	3.67	11.87	13.47	32.21	32.86
	Airplane mode	3.66	11.83	13.43	32.21	32.82
Ref. 21		3.78	12.32	13.57	32.19	33.76

Table 5: Frequencies of drive train system (configuration 1 and 3), unit: Hz.

Config.	Mode	f_1	f_2	f_3	f_4	f_5
1	Helicopter mode	7.71	8.87	12.39	12.40	227.67
	Airplane mode	7.71	8.87	12.39	12.40	227.11
3	Helicopter mode	3.78	12.13	13.57	32.19	33.79
	Airplane mode	3.78	12.13	13.56	32.18	33.75

7. Massimo Biggi, Pierre Abdel Nour, and Giorgio Vicenzotti. Next generation civil tiltrotor technology demonstrator program: Towards flight test. In *AIAA SCITECH 2024 Forum*, page 1491, Orlando, FL, USA, January 8–12 2024. https://doi.org/10.2514/6.2024-1491.

8. Susan A Gorton, Isaac Lopez, and Colin Theodore. NASA technology for next generation vertical lift vehicles. In *56th AIAA/ASCE/AHS/ASC Structures, Structural Dynamics, and Materials Conference*, page 0949, Kissimmee, FL, USA, January 5–9 2015. https://doi.org/10.2514/6.2015-0949.

9. Mark A. Stevens, David G. Lewicki, and Robert F. Handschuh. Concepts for multi-speed rotorcraft drive system-status of design and testing at NASA GRC. In *American Helicopter Society (AHS) 71st Annual Forum*, Virginia Beach, VA, USA, May 5–7 2015. https://doi.org/10.4050/F-0071-2015-10243.

10. Riccardo Bianco-Mengotti, Luca Medici, Carlo Cassinelli, Cristian Lilliu, Luca Viganò, Matteo Pecoraro, and Luca Sampugnaro. ATA: the advanced tiltrotor aircraft by LEONARDO. In *51st European Rotorcraft Forum*, Venice, Italy, September 9–11 2025. Paper no. 136.

11. Vincenzo Muscarello, Luigi Cocco, Marco Favale, Pierangelo Masarati, and Giuseppe Quaranta. Novel approach to interaction between engine-drive train system and deformable rotorcraft airframes. In *AHS 73rd Annual Forum*, Fort Worth, TX, USA, May 9-11 2017. https://doi.org/10.4050/F-0073-2017-12058.

12. Alberto Rigo, Vincenzo Muscarello, Pierangelo Masarati, Giuseppe Quaranta, and Marco Favale. Drive train modeling effects on tiltrotor aeroelastic analysis. In *Dynamics Specialists: Towards Flutter-Free Tiltrotors - the Next Generation - 2019 AIAA SciTech Forum*, San Diego, CA, USA, January 7–11 2019. https://doi.org/10.2514/6.2019-1367.

13. H. Holzer. *Die Berechnung der Drehsenwingungen*. Springer, Berlin, 1921.

14. N. O. Myklestad. New method of calculating natural modals of coupled bending-torsion vibration of beams. *Trans. ASME*, 67(1):61–67, 1945. https://doi.org/10.1115/1.4018171.

15. X. Rui, B. He, Y. Lu, W. Lu, and G. Wang. Discrete time transfer matrix method for multibody system dynamics. *Multibody System Dynamics*, 14(3–4):317–344, 2005. https://doi.org/10.1007/s11044-005-5006-1.

16. Xiaoting Rui, Guoping Wang, and Jianshu Zhang. *Transfer Matrix Method for Multibody Systems — Theory and Applications*. John Wiley & Sons, Singapore Pte. Ltd., 2019.

17. Xiao Wang, Laishou Song, and Pinqi Xia. A novel modeling strategy for the dynamical analysis of coupled coaxial rotors/auxiliary propeller/drive train system. *Journal of the American Helicopter Society*, 68(1):012003–1–15, 2023. https://doi.org/10.4050/JAHS.68.012003.

18. Bo Li, Xiao Wang, Pierangelo Masarati, and Yousong Xu. A novel modeling framework for tiltrotor coupled drivetrain dynamics. *Chinese Journal of Aeronautics*, Available online 14 July 2025. https://doi.org/10.1016/j.cja.2025.103666.

19. Jr. C. W. Acree. An improved CAMRAD model for aeroelastic stability analysis of the XV-15 with advanced technology blades. TM 4448, NASA, 1993.

20. M. Maisel. NASA/Army XV-15 tilt-rotor research aircraft familiarization document. TM X-62,407, NASA, January 1975.

21. Stefania Tonetti and Pierangelo Masarati. Graph-Based Modeling of Nonhomogeneous One-Dimensional Multibody Systems With Arbitrary Topology. *Journal of Computational and Nonlinear Dynamics*, 6(3):031011, July 2011.

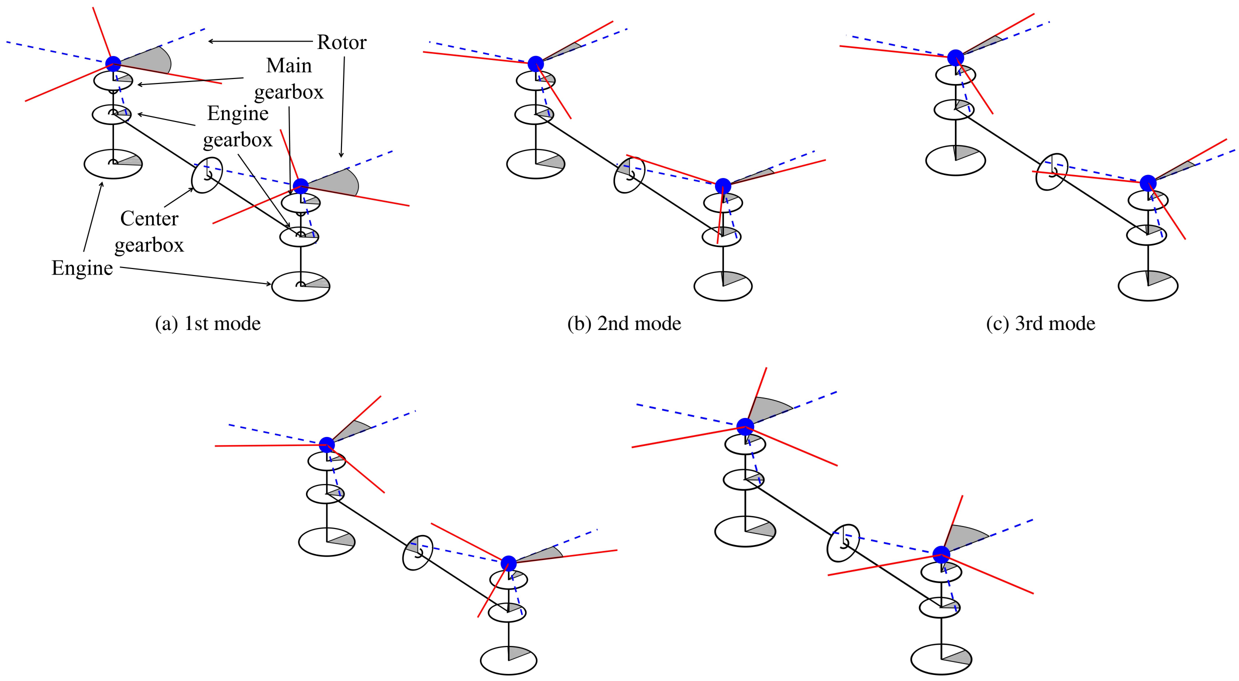

(a) 1st mode (b) 2nd mode (c) 3rd mode

(d) 4th mode (e) 5th mode

Figure 8: Mode shapes of drive train system (configuration 2) in helicopter mode.

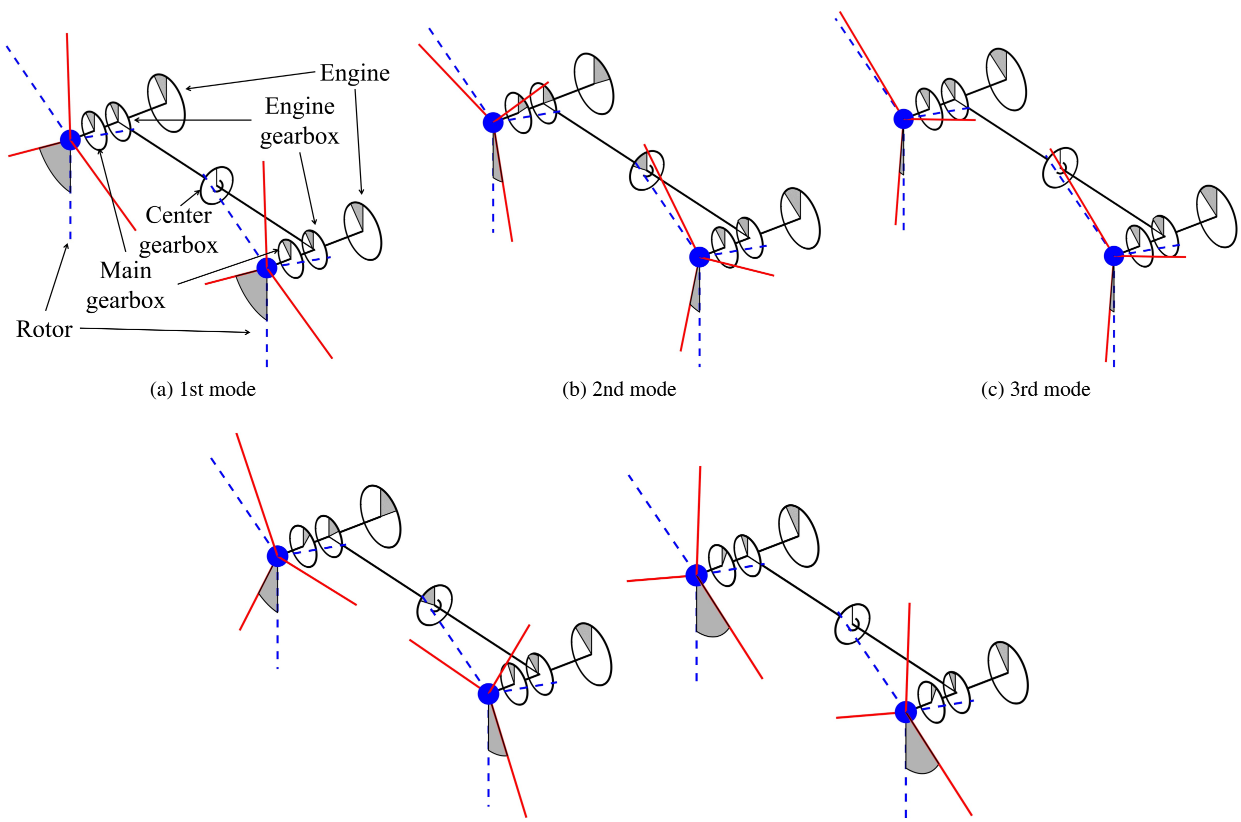

(a) 1st mode (b) 2nd mode (c) 3rd mode

(d) 4th mode (e) 5th mode

Figure 9: Mode shapes of drive train system (configuration 2) in airplane mode.

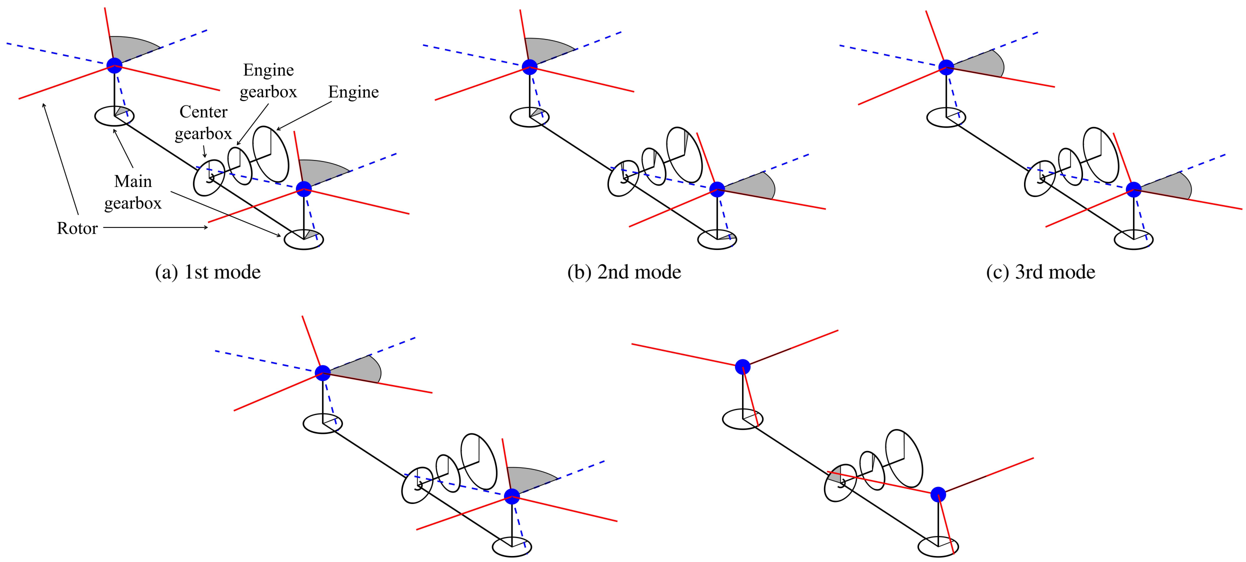

(a) 1st mode (b) 2nd mode (c) 3rd mode

(d) 4th mode (e) 5th mode

Figure 10: Mode shapes of drive train system (configuration 1) in helicopter mode.

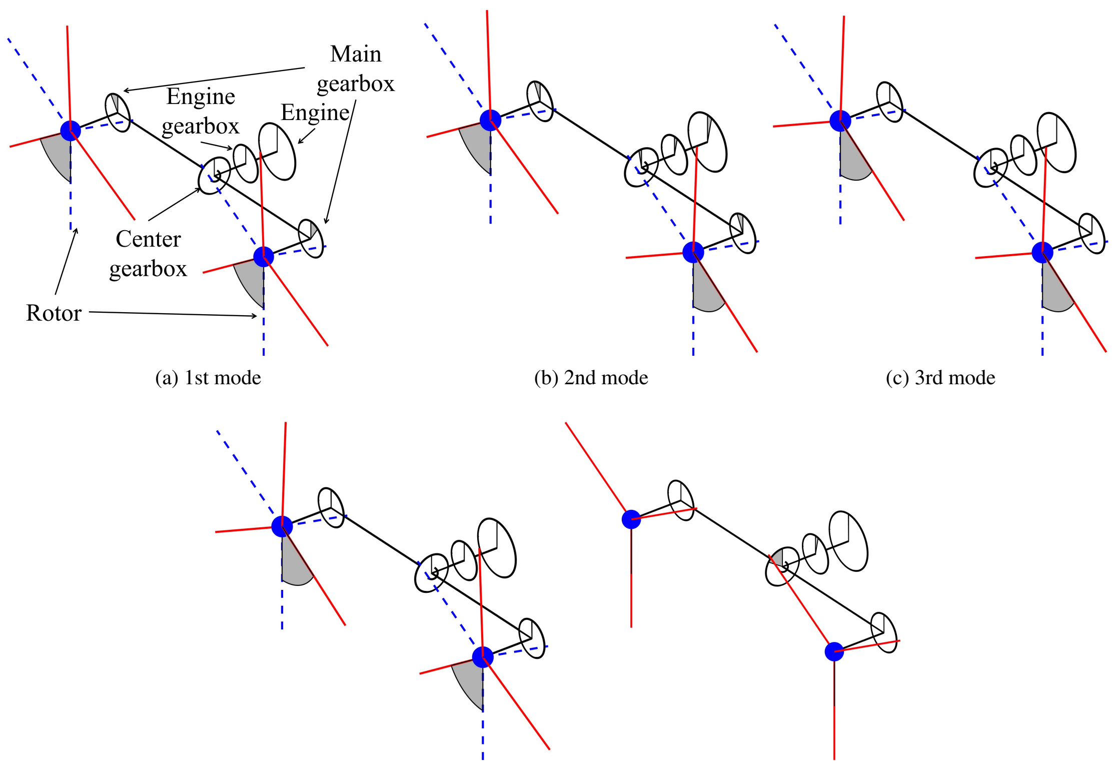

(a) 1st mode (b) 2nd mode (c) 3rd mode

(d) 4th mode (e) 5th mode

Figure 11: Mode shapes of drive train system (configuration 1) in airplane mode.

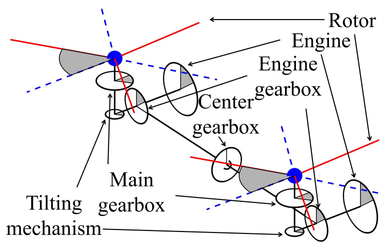

(a) 1st mode

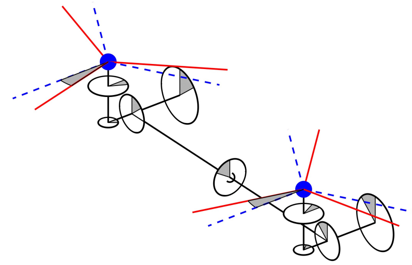

(b) 2nd mode

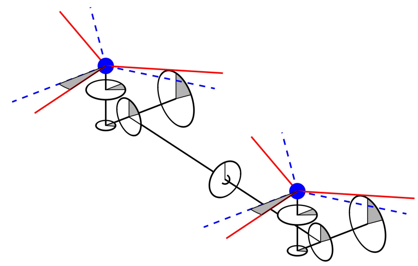

(c) 3rd mode

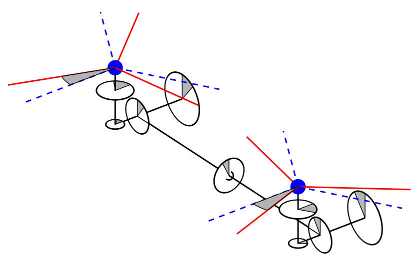

(d) 4th mode

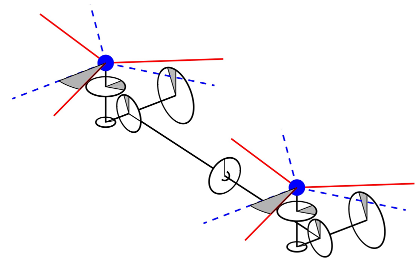

(e) 5th mode

Figure 12: Mode shapes of drive train system (configuration 3) in helicopter mode.

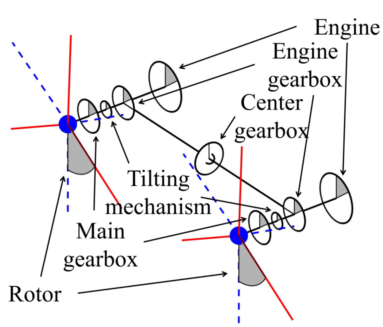

(a) 1st mode

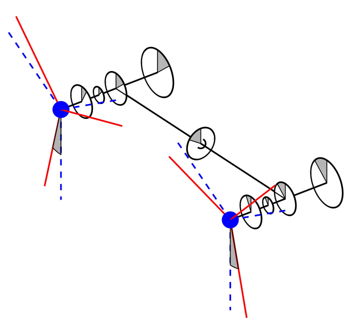

(b) 2nd mode

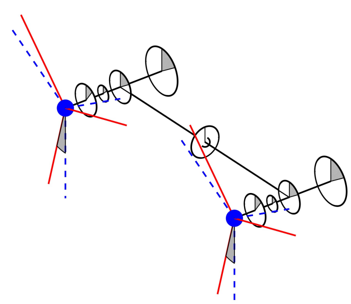

(c) 3rd mode

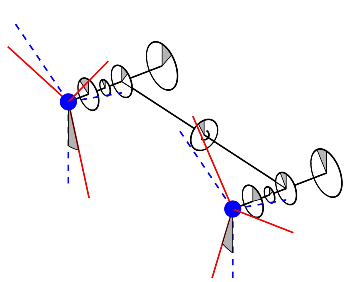

(d) 4th mode

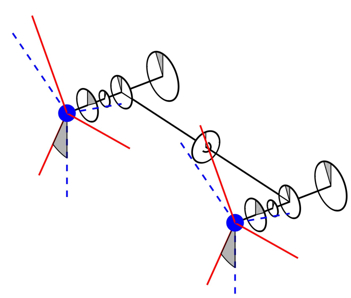

(e) 5th mode

Figure 13: Mode shapes of drive train system (configuration 3) in airplane mode.